THERMAL EXPANSION AND STRUCTURAL BEHAVIOR OF A CLOSED LOOP THERMAL WIND TUNNEL FOR ORC FLUIDS

Maximilian Passmann, Karsten Hasselmann,
Felix Reinker, Stefan aus der Wiesche

Department of Mechanical Engineering
Muenster University of Applied Sciences,
48565 Steinfurt, Germany
e-mail: f.reinker@fh-muenster.de

ABSTRACT

The Organic Rankine Cycle (ORC) offers great potential for recovering waste heat and using low-temperature sources for power generation. However, the ORC thermal efficiency is limited by the relatively low temperature level, and therefore, designing ORC components with high efficiencies and minimized losses is of major importance. The use of organic fluids creates new challenges for turbine and component design, due to dense gas behavior and the low speed of sound leading to high Mach numbers.

Computational fluid dynamics (CFD) offers great potential for design and optimization of ORC components. But the employment of CFD methods requires careful validation by means of experimental data. For ORC components, such an experimental approach requires the use of specially designed wind tunnels for organic vapors.

The closed wind tunnel, presented in this contribution, is designed as a pressure vessel system to allow for pressure levels up to p = 10 bars and temperatures up to θ = 180°C. The investigation of heavy weight organic fluid flows at superheated state also needs for higher temperature levels. Heating and cooling units are therefore used to achieve steady state conditions inside of the test section.
In this contribution the design process of a closed loop wind tunnel is presented, focusing on the thermal expansion of the system. Thermal finite element method (FEM) analysis is applied to calculate temperature distributions, considering thermal loads and heat losses of the facility. Based on these data, linear FEM analysis is used to investigate thermal stress in the closed loop vessel system. Supporting points and critical zones are assessed in a more detailed analysis. A method to analyse the transient behavior of the structure and to determine allowable heating rates during heat-up phase is presented.

The testing facility is part of a large research project aiming at obtaining loss correlations for performance predictions of ORC turbines and processes, which is supported by the German Ministry for Education and Research (BMBF).

1. INTRODUCTION

The Organic Rankine Cycle represents a viable technical approach for conversion of low temperature sources, like waste heat or geothermal reservoirs, to electricity or to combined electricity and heat. An ORC process consists of a Rankine cycle employing an organic compound as working fluid. This technology is usually preferred over steam cycles, due to the higher thermodynamic cycle efficiency, in case of low-grade heat sources [1, 4, 9]. The design and performance prediction of steam and gas turbines have been initially based on measurements and numerical simulations of flow through two-dimensional cascades of blades [5]. In case of ORC turbines and related fluids, such an approach requires the use of specially designed wind tunnels and dedicated instrumentation. The Laboratory for Thermal and Power Engineering of Muenster University of Applied Sciences, Germany is building up

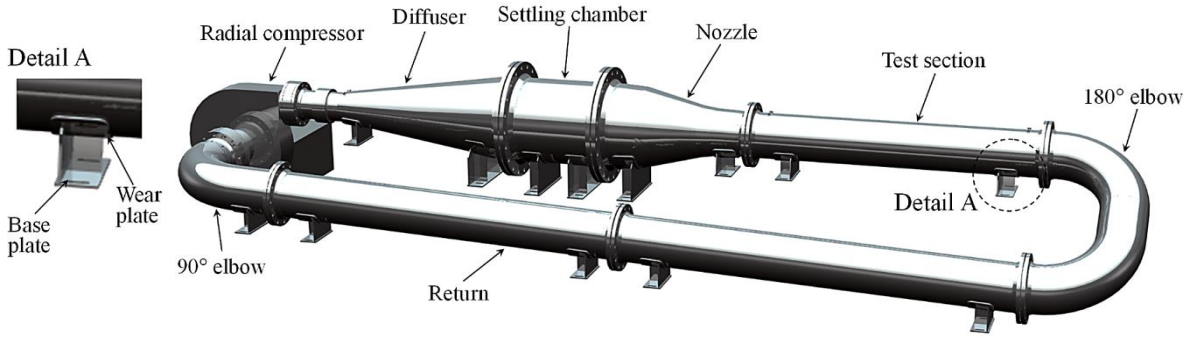

Figure 1: 3D model of the closed circuit wind tunnel for ORC fluids.

a closed loop wind tunnel for investigating real gas effects in dense gas flows of organic vapors in nozzles and axial turbine blades.

The basic test section, as shown in Fig. 1, acts as a barrel-type casing allowing for different inserted test sections like simple nozzle geometries or axial turbine blade test sections. The maximum Mach number upstream the blade section will lie in the transonic region (M = 1). Shadow schlieren visualization utilizing a high speed camera will be used for qualitative flow characterization in the test section. For local flow field investigation Laser Doppler Anemometry will be used. Besides optical measurements, classical pneumatic measurement techniques will also be performed, as for instance to measure the pressure field alongside the nozzle axis.

Subject of the present contribution is the examination of thermal expansion and structural behavior of the facility by means of structural and thermal linear finite element analysis. Fig. 1 shows a 3D model of the closed circuit wind tunnel in its current development status. To allow for operating conditions of up to p = 10 bars internal pressure at θ = 180°C, all pressurized components are laid out according to pressure rating PN16 [13]. The support saddles (cf. Fig. 1, detail A) are designed on the basis of DIN 28080 [6] with a wall thickness of 10 mm for the wear plate and 8 mm for all other components. The entire unit rests on a rigid steel subframe (not shown in Fig. 1). The saddle base plates act as bearing areas. Sliding plates will be installed between subframe and base plates, to reduce friction forces and to avoid thermal bridging to the ground.

The dimensions of the wind tunnel are approximately 7200 mm in length and 1600 mm in width. The 180° elbow is angled at 30°, resulting in a maximum level difference of 610 mm between test section and return. An overview of the dimensions is given in Tab. 1.

The first part of this paper focuses on the overall bearing concept of the unit, taking into account thermal and structural influences. A simplified shell model is used to investigate three different bearing concepts under steady-state conditions. In the second part, temperature distribution and thermal stress, occurring during heat-up phase, will be addressed based on the example of the settling chamber.

Table 1: Dimensions of the closed circuit wind tunnel for ORC fluids.

Component	**Length**	**Midsurface diameter**		**Wall thickness**
	l [mm]	d_{min} [mm]	d_{mout} [mm]	s [mm]
Diffuser	1745	216.1	601.2	8.8
Settling chamber	690	601.2		8.8
Nozzle	1073	601.2	318.5	8.8
Test section	2067	318.5		7.1
Return	5454.3	318.5		7.1
	Radius	**Midsurface diameter**	**Length in x-direction**	**Length in y-direction**
	r [mm]	d_m [mm]	l_x [mm]	l_y [mm]
90° elbow	486	318.5	648	486
180° elbow	486	318.5	1221	564

2. FINITE ELEMENT ANALYSIS OF THE STATIC SHELL MODEL

2.1 Finite Element Model

Linear finite element analysis utilizing NX Nastran version 8.5 (SOL101) [10] is used to investigate expansion and stress distribution resulting from both, thermal and structural loads under steady-state conditions. Based on the 3D solid model of the wind tunnel, as depicted in Fig. 1, a midsurface model was generated. Mapped meshing was utilized to mesh the midsurface with 8-noded shell elements (CQUAD8). For singly curved shells like cylinders this element type performs better than the 4-noded CQUAD4 element [10]. The coordinate system and calculated stresses for this type of element are shown in Fig. 2. CQUAD8 elements are isoparametric with four corner and four mid-side grid points. Stresses, as shown in Fig. 2, are evaluated at the centroid and at the vertices. For plane strain analysis the von Mises equivalent stress σ_{VFEM} is defined by:

$$\sigma_{VFEM} = \sqrt{\frac{1}{2} \cdot \left[\left(\sigma_x - \sigma_y\right)^2 + \left(\sigma_y - \sigma_z\right)^2 + \left(\sigma_z - \sigma_x\right)^2 \right] + 3 \cdot {\tau_{xy}}^2} \qquad (1)$$

with the stress component in z-direction being $\sigma_z = 0$. A thorough description of the finite element method and theoretical backgrounds concerning shell elements can be found in [3].

Multiple mesh collectors were generated, to account for different wall thicknesses and materials in pipe sections and support saddles. The meshed model is shown in Fig. 3. The pressure vessel is made from high-alloy austenitic steel (X5CrNi18-10), whereas the support saddles are made from construction steel. For both materials all physical and mechanical properties were implemented into NX as temperature dependent values [12]. Typical values are given in Section 2.2.

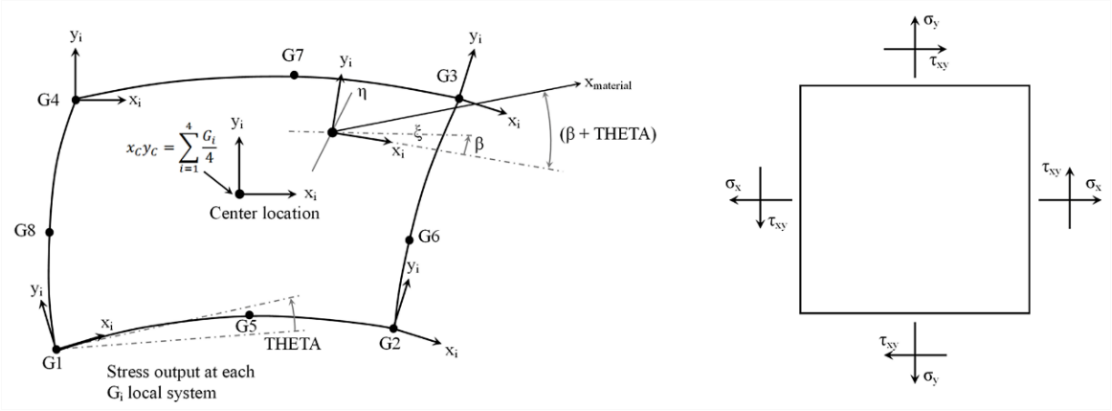

Figure 2: CQUAD8 coordinate system and stresses in shell elements.

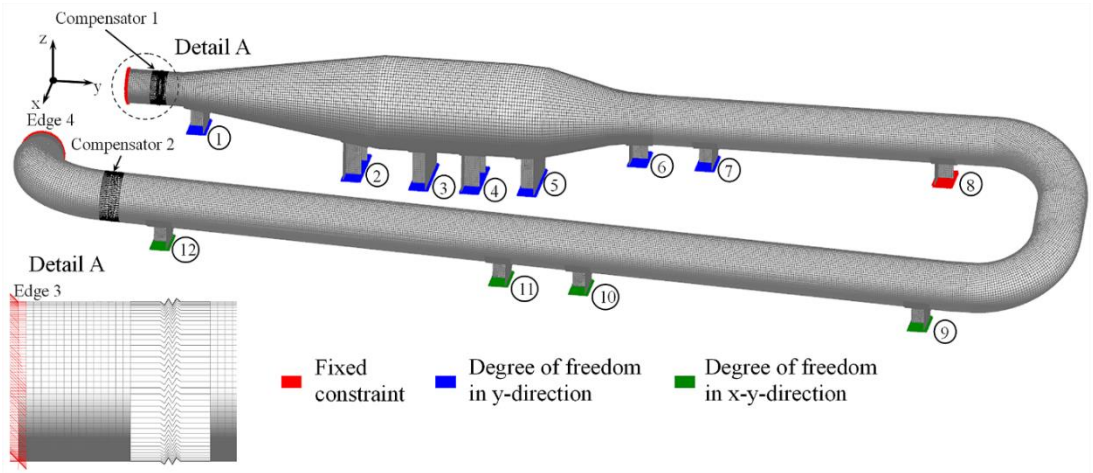

Figure 3: Meshed finite element shell model with boundary conditions.

The two axial compensators were modeled with elastic 1D elements (CELAS) which behave like simple extension or compression springs (cf. Fig. 3, detail A). The axial spring stiffness for compensator 1 and 2 were assumed as k = 257 N/mm and k = 705 N/mm respectively.

A surface-to-surface glue constraint was applied to connect each wear plate of the saddle to the pressure vessel. Glue constraints allow to join dissimilar meshes by creating weld-like connections, preventing relative motion in all directions between the glued surfaces. At the same time, displacements and loads are transferred correctly, resulting in an accurate strain and stress condition between glued surfaces [10].

The boundary conditions were modeled according to Fig. 3. All nodes on edge 3 and 4 representing the connection between pressure vessel and radial compressor were fixed, as was the lower face of the base plate of saddle 8. Support saddles 1 to 7 act as movable bearing points with a single degree of freedom (DOF) in x-direction at the lower face of the saddle base plates. For the remaining saddles 9 to 12 the base plates were fixed in all degrees of freedom but in x- and y-direction. This concept was modified later on as described in Section 2.3. The entire vessel was loaded with p = 10 bars internal pressure and a temperature of θ =180 °C.

2.2 Material Properties

Two materials were used in the simulation. The pressure vessel whose inner surface is in contact with the organic fluid is made from X5CrNi18-10. The support saddles are made from construction steel. The temperature dependency of mechanical and physical properties are taken into account in the finite element model. Typical values for both materials at θ = 20°C and θ = 180°C are given in Tab. 2.

The decisive strength parameter for both X5CrNi18-10 and construction steel is the yield strength $R_{p0.2}$ which is depicted in Fig. 4 as function of temperature θ. Especially in the case of X5CrNi18-10, the operating temperature of θ = 180°C leads to a significant decrease in strength, resulting in a value of $R_{p0.2}$ = 131 N/mm² compared to a nominal value of $R_{p0.2}$=190 N/mm² at θ = 20°C.

Table 2: Mechanical and physical properties of construction steel and X5CrNi18-10 at θ = 20°C and θ = 180°C.

Material	Temperature	Density	Young's module	Yield strength	Coefficient of linear expansion
	θ	ρ	E	$R_{p0.2}$	α
	[°C]	[kg/m³]	[N/mm²]	[N/mm²]	[10^{-6} K^{-1}]
Construction steel	20	7830	207000	140	11
	180	7830	207000	134	12.3
X5Cr-Ni18-10	20	7900	200000	190	16
	180	7900	186000	131	17

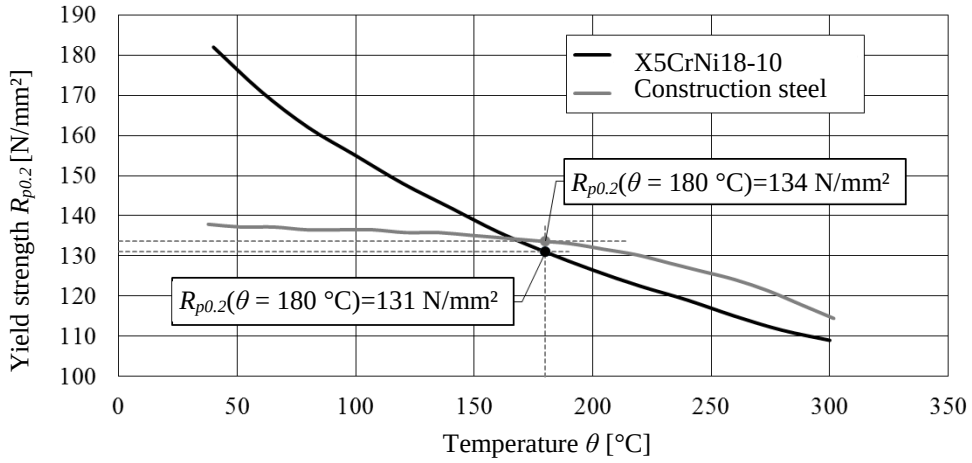

Figure 4: Temperature dependency of yield strength $R_{p0.2}$ for construction steel and X5CrNi18-10.

2.3 Results of the Static Shell Model

The decisive strength parameter for evaluating the results is the allowable stress at design temperature σ_{aDT}, with the yield strength $R_{p0.2}$ at design temperature and the safety factor S = 1.5 according to [13]:

$$\sigma_{aDT} = \frac{R_{p0.2}}{S}\,. \tag{2}$$

For the given temperature of θ = 180°C the allowable stress for X5CrNi18-10 results in a value of approximately σ_{aDT} = 90 N/mm². One-dimensional thermal expansion can be estimated for a given temperature difference $\Delta\theta$, thermal expansion coefficient α, and geometric dimension l from [8]:

$$\Delta l = \alpha \cdot l \cdot \Delta\theta \tag{3}$$

with values for α according to Tab. 2 and dimension l according to Tab. 1.

Three different bearing-concepts were investigated (cf. Tab. 3). Starting point for the calculations was concept a) as shown in Fig. 3. The position of saddles 8, 9 and 13 are shown in Fig. 6. For concepts a) and b) only saddles 8 and 9 were considered. In concept c) an additional saddle 13 was added in front of the 90° elbow.

Fig. 5 shows the effects of temperature, pressure and the combination of both on nodal displacements. The basis for this calculation is concept a). In the first step, only a temperature load of θ = 180°C was applied to the structure (cf. Fig. 5, left side). The resulting displacements in x- and y-direction are consistent with analytical values calculated from Eq. 3. In the second step, only an internal pressure load of p = 10 bars was applied to all pressurized parts (cf. Fig. 5, in the middle). The resulting radial stresses in the test section, diffuser, settling chamber, and nozzle compare well to the analytical values derived from standard equations as found for instance in [8, 13]. However, the major effect of the pressure load is the tendency to bend up the 180° elbow. This movement is allowed due to the fact that saddles 9 to 12 of the return section have DOFs in x- and y- direction, while saddle 8 of the test section is fixed. Therefore, the axial compensator of the return section with its low spring stiffness of k = 705 N/mm offers little resistance and acts as an extension spring. The resulting maximum displacements in the 180° elbow lie in the order of 20 mm.

In a final step the combination of temperature and pressure loads were considered (cf. Fig. 5, right side). Both individual influences can be superimposed [11]. While the tendency to straighten up the 180° elbow remains, the expansion of the axial compensator is substantially reduced. This can be attributed to the fact that the displacement of the return section, resulting from the thermal load, is in reverse direction to the displacement caused by internal pressure. The main portion of the resulting strain can be attributed to the effect of pressure. High values of strain can result in critical stress values especially in the area of the 180° elbow. Fig. 6 shows displacement and resulting stress values for different bearing concepts. For each of the three evaluated concepts the bearing concept was gradually modified to optimize strain and stress distribution. Each time the structure was loaded with a temperature of θ = 180°C and internal pressure of p = 10 bars. Average and maximum stress values for 180° elbow, return, 90° elbow, and test section are shown in Fig. 7.

Table 3: Bearing concepts for the static shell model.

Saddle	**8**	**9**	**13**
	Degree of freedom (DOF)		
Concept a)	fixed	x-y	-
Concept b)	fixed	x	-
Concept c)	fixed	x	x

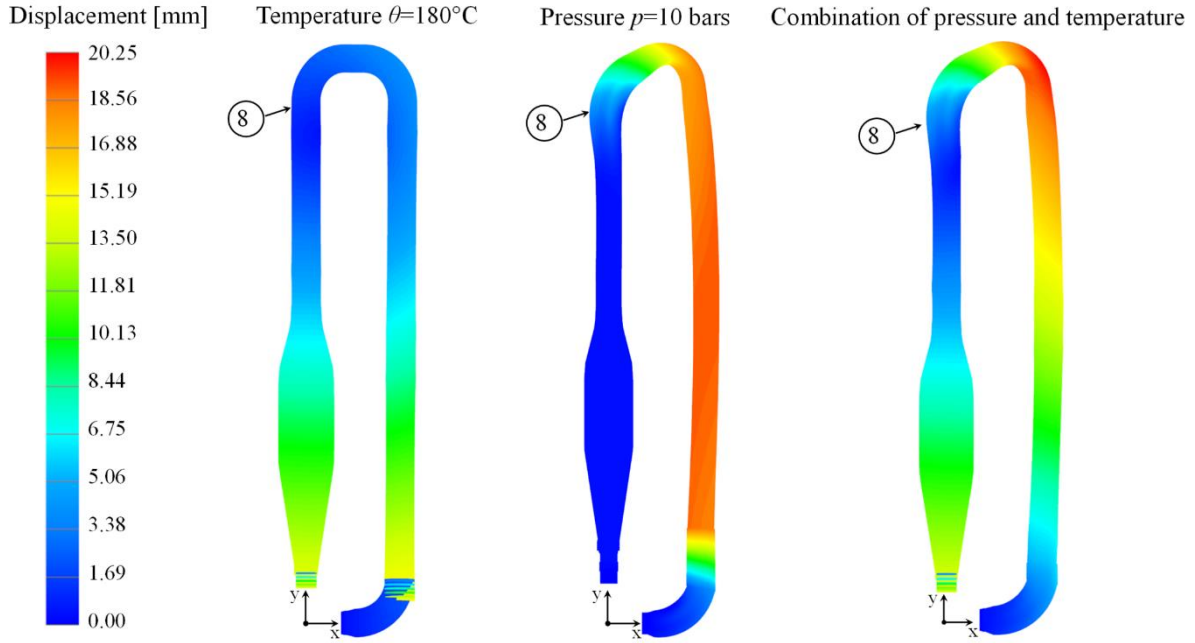

Figure 5: Effect of temperature and pressure on displacement for the basic model as shown in Figure 3.

For concept a) saddle 8 at the end of the test section was fixed. All saddles at the return section have DOFs in x- and y- direction. The results are high values of stress in the 180° elbow, test section and return. The maximum stress values in all four sections exceed the allowable stress of σ_V = 90 N/mm² by a factor of 1.3 up to 2.4. For concept b) saddle 9 in addition to saddle 8 was fixed in y-direction to prevent the tendency to straighten up the 180° elbow, allowing only for movement in x-direction. As a result, average and maximum stress values found in the 180° elbow, test section and return are greatly reduced and lie below the allowable stress level. With a maximum of σ_V = 144 N/mm² in the 90° elbow, concept b) still leads to an overloading of this section. Therefore, saddle 13 was added for concept c). By locking the DOF in y-direction, the reaction force of the axial compensator is no longer affecting the 90° elbow but is absorbed by the saddle. The resulting maximum stress of σ_V = 79.7 N/mm² was almost halved compared to the σ_V = 144.4 N/mm² from concept b).

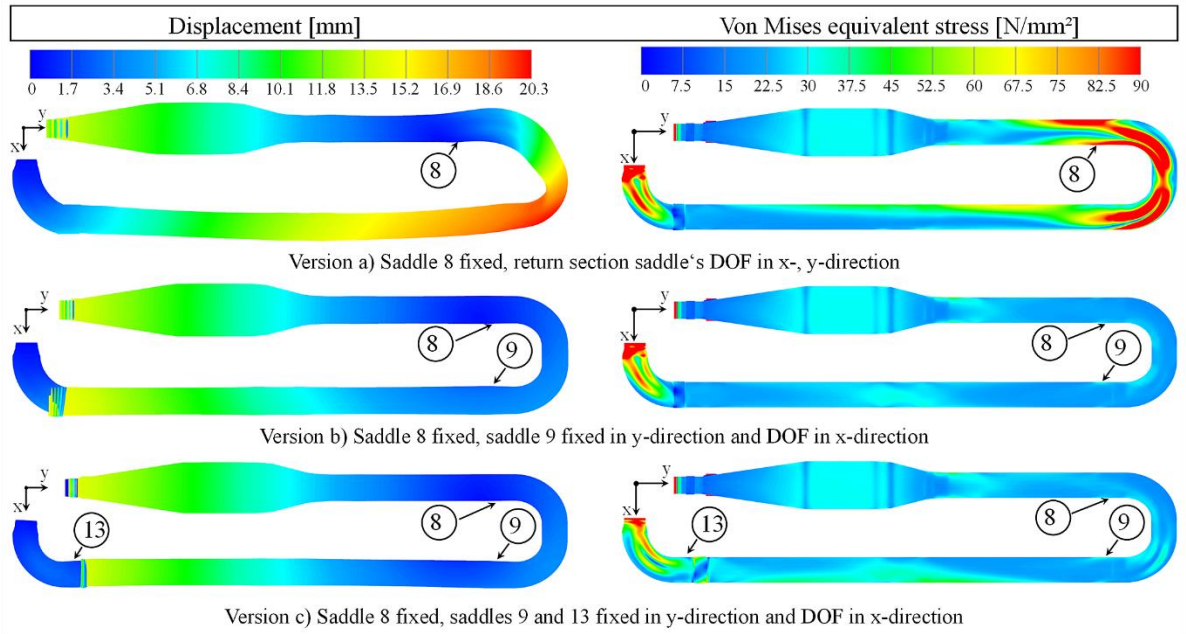

Figure 6: Effect of different bearing-concepts on displacement and von Mises stress.

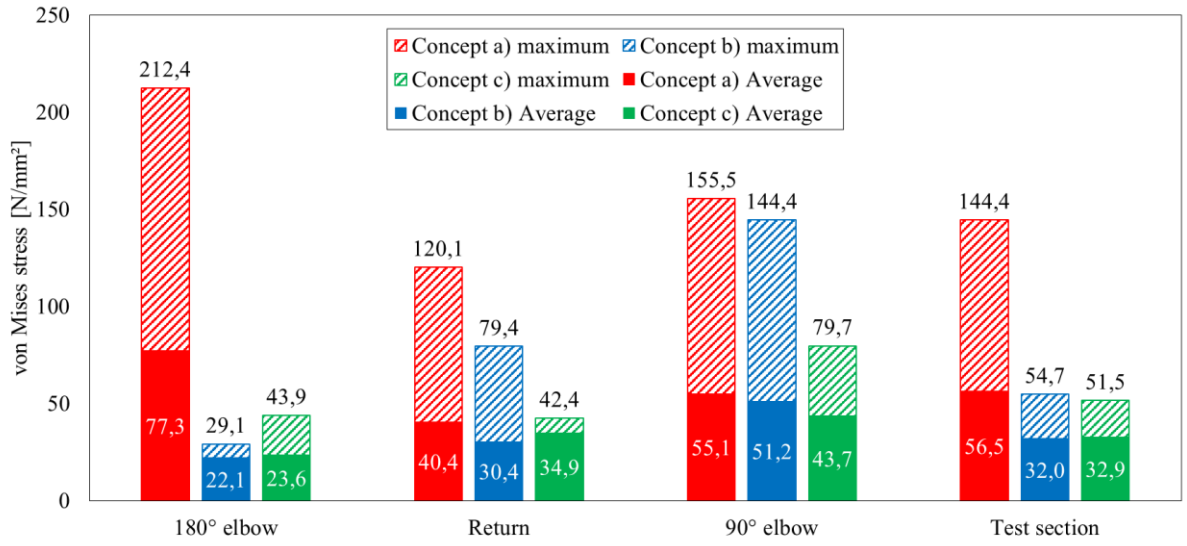

Figure 7: Maximum and average von Mises equivalent stress for concepts a), b) and c).

3. TRANSIENT ANALYSIS

During the start-up process, thick-walled parts and areas of high material accumulation lead to significant temperature differences within the material. The resulting thermal strain evokes high residual stress states [11]. In general, thermal stresses are directly proportional to the temperature difference (θ_i-θ_m) of a local temperature θ_i to the average wall temperature θ_m. Thermal stresses are also known to be proportional to the square of the wall thickness. Therefore, thick-walled components usually determine allowable heating and load change rates [11]. Thermal expansion and resulting thermal stresses during heat-up phase were investigated using the example of the settling chamber, which was assumed to be critical due to its massive flanges.

Analytical methods for estimating the maximum temperature differences and resulting thermal stresses exist for simple geometries like spheres, cylinders or plates [2, 11]. Applying the procedure given by [2], the progression of the wall temperature difference (θ_i-θ_m) in a plate, resulting from a sudden temperature change, was plotted over a period of two hours (cf. Fig. 8). According to Fig. 8, the maximum temperature difference hence the maximum thermal stress in a plate will occur within the first 30 minutes. Assuming a similar transient behavior for the settling chamber, the following investigations were confined to a time frame of 60 minutes.

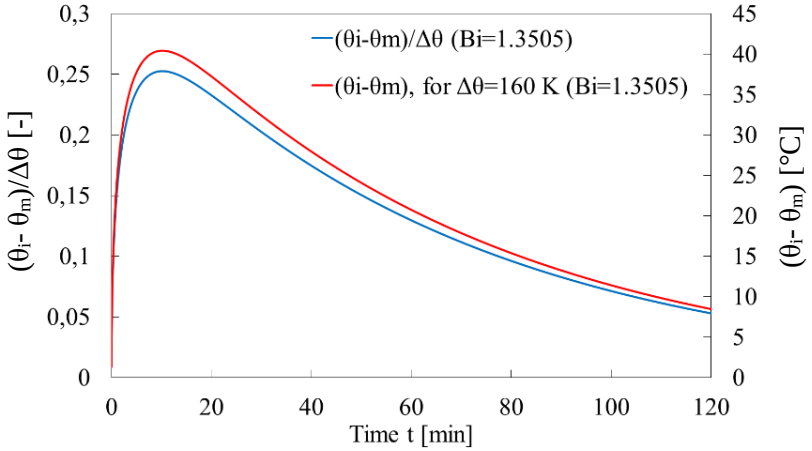

Figure 8: Wall temperature difference over time for a sudden temperature change in a plate.

3.1 Finite Element Model for Transient Analysis

In the First step, a thermal finite element model was built, which provided the temperature distribution throughout the structure. This was achieved using the NX Thermal solver in advanced transient settings [7]. In an interim step, a mapping solution mapped the nodal temperatures to the structural model, which in turn provided strain and stress distribution. For the structural computations linear finite element analysis utilizing NX Nastran (SOL 101) was used. Symmetry to the y-z-plane was exploited for all models to reduce computing time.

The thermal model, as shown in Fig. 9 on the left hand side, was meshed with 4-noded tetrahedral elements. As the whole structure will be insulated with a layer of mineral wool, a solid body of 100 mm thickness was added. The introduction of heat into the structure will be achieved by electric heating sleeves applied to the pressure vessel. A thermal load was applied to the outer surface of the pressure vessel to model the heating sleeves (cf. Fig. 9, Detail A), assuming the thermal resistance between heating sleeves and pressure vessel to be negligibly small. The thermal load is regulated by a PID controller with a specified target temperature of θ = 180°C. A number of elements from the mesh of the pressure vessel were chosen as sensors for the controller. Natural convection at the outer surface of insulation and saddle was added utilizing built in correlations provided by NX for cylinder, horizontal and vertical plate. The assumed ambient temperature is θ = 22°C. As the pressure vessel will be under vacuum during the start-up process, the inner surface of the vessel is adiabatic in this model.

The structural model was meshed utilizing mapped meshing with 20-noded hexahedral elements. Mesh refinement was carried out in the area of the pressure vessel, to ensure 4 element layers across the wall thickness. The bended wear plate of the saddle was meshed with 10-noded tetrahedral elements. In the symmetry y-z-plane a symmetrical constraint was applied (DOF in y- and z-direction). At the right end of the model the raised surface of the flange (flange gasket contact area) was fixed. The cross section of the pressure vessel at the left end was elastically supported by grounded springs. The springs represent the axial compensator with a spring stiffness of k = 257 N/mm.

For the pressure vessel and saddle the same materials as described in Section 2.1 were used. The thermal model additionally contains the insulation layer. A material file was generated using physical properties of mineral wool assuming isotropic material behavior. Mineral wool possesses an average thermal conductivity of λ = 0.05 W/(m·K), a density of ρ = 100 kg/m³ and a specific heat capacity of c_p = 0.84 kJ/(kg·K) [12].

3.2 Results of the Transient Analysis

Temperature distribution and thermal stress were evaluated for two different configurations over a period of 60 minutes. For configuration a) a thermal load of $\dot{q}$ = 2500 W/m² was applied to the outer surface of the pressure vessel as described in Section 3.1. For configuration b) the thermal load was split up into two

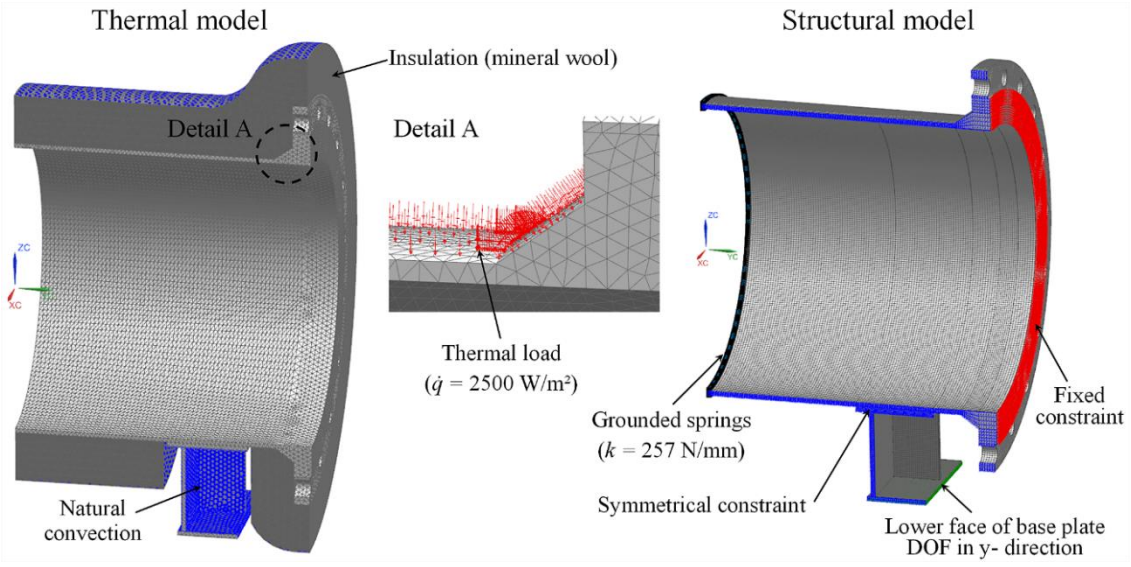

Figure 9: Meshed thermal and structural finite element model of settling chamber.

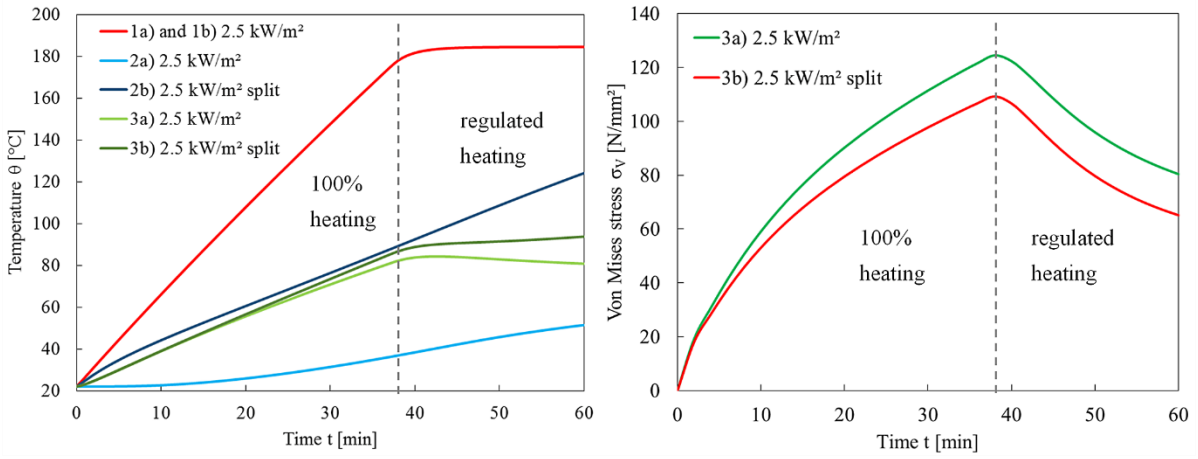

Figure 10: Development of temperature θ and von Mises stress σ_V over the first hour during heat-up phase for a thermal load of $\dot{q}$ = 2500 W/m² at different structural points.

areas. The first load was defined for the pressure vessel itself, whereas the second one only covered the surface area of the flange. The weld, joining pressure vessel and flange, was chosen as the parting line between the two areas. In this configuration each thermal load had its own PID controller assigned to it.

The development of temperature θ and von Mises stress σ_V within the first hour for a thermal load of $\dot{q}$ = 2500 W/m² is shown in Fig. 10. The positions of the points 1) to 3) are illustrated in Fig. 11. In the thin walled pressure vessel, represented by points 1a) and 1b), the temperature curve is identical for both configurations. After approximately 40 minutes this area has reached its target temperature of θ = 180°C. After that the PID controller reduces the thermal load to maintain the target temperature. A similar behavior can be observed for points 3a) and 3b).

The maximum stress values occur in the areas of the weld seam, joining pressure vessel and flange, and the weld seam, joining pressure vessel and saddle. As becomes evident from Fig. 10 (right hand side), configurations a) and b) both yield failure critical stress values of up to σ_V = 123 N/mm². However, by splitting up the thermal load and defining two separate areas a more uniform temperature distribution in vessel and flange can be achieved resulting in lower thermal stress values.

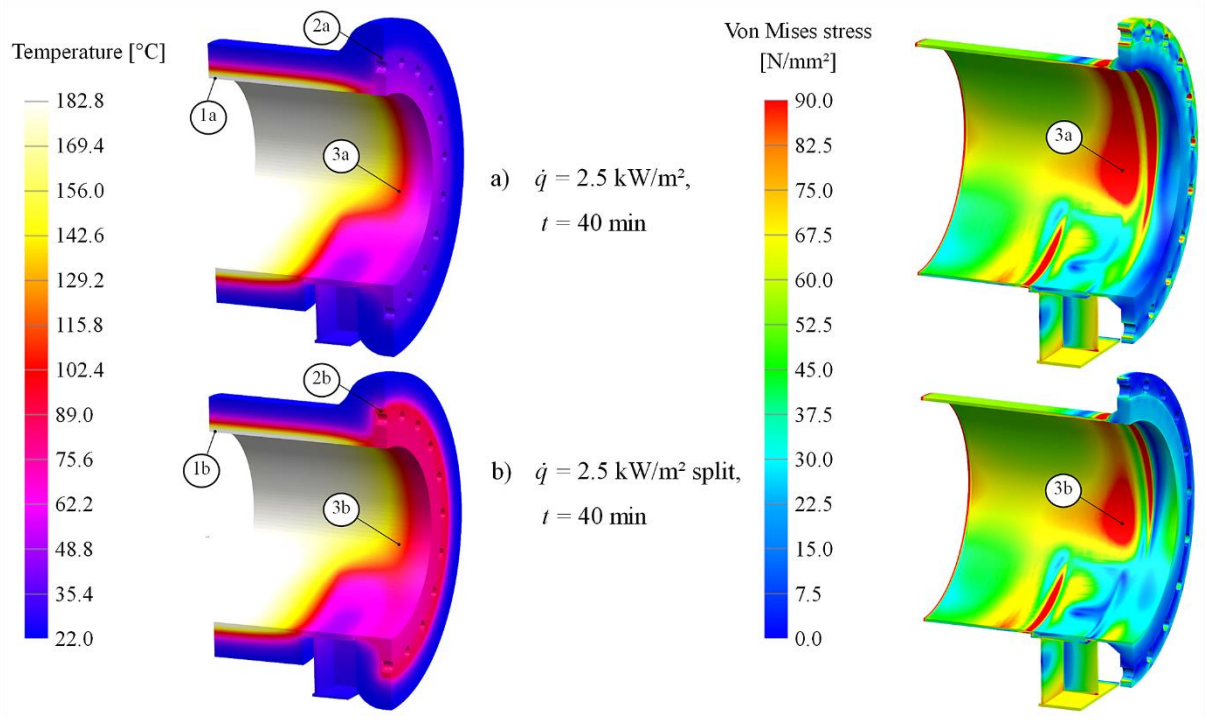

Figure 11: Temperature θ and von Mises stress σ_V distribution at t = 40 min for a thermal load of $\dot{q}$ = 2500 W/m².

4. CONCLUDING COMMENTS

This paper describes a method to design and analyse the bearing concept of a closed wind tunnel for organic fluids by means of linear finite element analysis. A simplified shell model was built up and three different concepts were considered. The basic impacts of temperature and pressure loads were identified. Based on these findings an optimized bearing concept, leading to an equal strain and stress distribution, was developed.

Temperature distribution and thermal stress during heat-up phase were investigated using combined thermal and structural finite element analysis. The thermal model provided transient temperature distributions, which were used to calculate thermal stresses. A method was presented to reduce these thermal stresses by way of achieving a uniform temperature distribution throughout the structure. As the resulting stress values presented in this paper are still above the critical yield strength, further investigations are needed. This includes the determination of permitted heating rates, the ideal configuration of the heating sleeves and their individual regulation.

5. NOMENCLATURE

c_p	Specific heat capacity	kJ/(kg·K)
d_m	Midsurface diameter	mm
E	Young's modulus	N/mm²
k	Spring stiffness	N/mm
l	Length	mm
$\dot{q}$	Heat flux	W/m²
r	Radius	mm
$R_{p0.2}$	0.2%-yield strength	N/mm²
s	Wall thickness	mm
t	Time	s
α	Coefficient of linear expansion	1/K
θ	Temperature	K
ρ	Density	kg/m³
σ_V	Von Mises equivalent stress	N/mm²
τ	Shear stress	N/mm²

6. REFERENCES

[1] Adam, A. W., ed., 1995. *Organic Rankine Cycles. Encyclopedia of Energy Technology and the Environment*, John Wiley & Sons, New York, 3024 p.

[2] Baehr, H.D., Stephan, K., 2013. *Wärme- und Stoffübertragung*, Springer, Berlin, Heidelberg, 804 p.

[3] Bathe, K.J., 2002. *Finite Elemente Methode*, Springer, Berlin, Heidelberg, 1253 p.

[4] Chen, H., Goswami, D. Y., and Stefanakos, E. K., 2010. *A review of thermodynamic cycles and working fluids for the conversion of low-grade heat*, Renewable and Sustainable Energy Reviews, 14(9), pp. 3059-3067.

[5] Dixon, S. L., 1998. *Fluid mechanics and thermodynamics of turbomachinery*, Butterworth-Heinemann, Boston, 556 p.

[6] German Institute for Standardization, 2003. *DIN 28080:2003-08, Saddle supports for horizontal apparatus - Dimensions*, Berlin, 12 p.

[7] Maya Heat Transfer Technologies Ltd., 2012. *NX Thermal Reference manual*, 544 p.

[8] Scholz, G., 2012. *Rohrleitungs- und Apparatebau*, Springer, Berlin, Heidelberg, 411 p.

[9] Schuster, A., Karellas, S., Kakaras, E., and Spliethoff, H., 2009. *Energetic and economic investigation of organic rankine cycle applications*, Applied Thermal Engineering, 29(8-9), pp. 1809-1817.

[10] Siemens Product Lifecycle Management Software Inc., 2012. *NX Reference manual.*

[11] Strauß, K., 2009. *Kraftwerkstechnik*, Springer, Berlin, Heidelberg, 522 p.

[12] VDI e.V., ed., 2013. *VDI-Wärmeatlas*, Springer, Berlin, Heidelberg, 1760 p.

[13] Verband der TÜV e.V., ed., 2006. *AD 2000 - Regelwerk*, Carl Heymanns Verlag, Berlin, 796 p.